Naval Research Laboratory

Washington, DC 20375-5000

NRL Memorandum Report 6429

A Complex Systems Approach to Metallic Fracture Surface Characterization

GEORGE C. KIRBY III AND PETER MATIC

Mechanics of Materials Branch
Materials Science and Technology Division

AD-A232 546

February 6, 1991

DTIC
ELECTE
MAR 12 1991
S B D

91 3 06 012

REPORT DOCUMENTATION PAGE

Public reporting burden for this collection of information is estimated to average 1 hour per response including the time for reviewing instructions searching existing data sources gathering and maintaining the data needed, and completing and reviewing the collection of information. Send comments regarding this burden estimate or any other aspect of this collection of information, including suggestions for reducing this burden to Washington Headquarters Services, Directorate for Information Operations and Reports, 1215 Jefferson Davis Highway, Suite 1204, Arlington, VA 22202-4302, and to the Office of Management and Budget, Paperwork Reduction Project (0704-0188), Washington, DC 20503

1. AGENCY USE ONLY (Leave blank)	2. REPORT DATE 1991 February 6	3. REPORT TYPE AND DATES COVERED

4. TITLE AND SUBTITLE
A Complex Systems Approach to Metallic Fracture
Surface Characterization

5. FUNDING NUMBERS
PE - 66153N
PR - RR022-01-48
WU - 480-509

6. AUTHOR(S)
George C. Kirby III and Peter Matic

7. PERFORMING ORGANIZATION NAME(S) AND ADDRESS(ES)
Naval Research Laboratory
Washington, DC   20375-5000

8. PERFORMING ORGANIZATION REPORT NUMBER
NRL Memorandum
Report 6429

9. SPONSORING/MONITORING AGENCY NAME(S) AND ADDRESS(ES)
Office of Naval Research
Arlington, VA   22217

10. SPONSORING/MONITORING AGENCY REPORT NUMBER

11. SUPPLEMENTARY NOTES

12a. DISTRIBUTION/AVAILABILITY STATEMENT
Approved for public release; distribution unlimited.

12b. DISTRIBUTION CODE

13. ABSTRACT (Maximum 200 words)
The physical scale of observation and the mathematical formation of description are important choices for the modeling of physical phenomena. The role of local interactions in relating complex features at different scales in inelastic material fracture is important since material damage has local origins while fracture is a large scale event. In this investigation, the relationship between large scale and small continuum scale fracture surface features are quantified in terms of local, small scale interactions. Experimental measurement of local fracture surface orientation were obtained from processing video images of the fracture surface under different illumination directions. The image processing mapped pixel intensities into a set of three local fracture surface inclination classes defined with respect to the macroscopic surface normal and crack growth direction.

14. SUBJECT TERMS		15. NUMBER OF PAGES 52
Fracture	Cellular automata	
Complex Systems	Video imaging	**16. PRICE CODE**
	Self-organization	

17. SECURITY CLASSIFICATION OF REPORT	18. SECURITY CLASSIFICATION OF THIS PAGE	19. SECURITY CLASSIFICATION OF ABSTRACT	20. LIMITATION OF ABSTRACT
UNCLASSIFIED	UNCLASSIFIED	UNCLASSIFIED	SAR

CONTENTS

A COMPLEX SYSTEMS APPROACH TO METALLIC FRACTURE SURFACE CHARACTERIZATION

Introduction

The physical scale of observation and the mathematical formalism of description are important choices for the modeling of physical phenomena. For continuous media, observations at different scales often demonstrate distinctly different and complex features. For the deformation, damage and fracture of solids, observations from the crystal lattice scale to the macroscopic component scale define the domain which theoretical and computational modeling address. Within these boundaries, quantitative relationships between any intermediate scales are valuable aids to theoretical modeling.

In this investigation, the geometry of the large scale fracture surface is examined in terms of its underlying relationship to smaller scale geometric features, quantified at approximately the continuum scale. The measurement of the smaller scale fracture surface topography, the analytical utilization of these measurements and the role of computational simulation are addressed in the course of demonstrating large scale structure on the fracture surface. This large scale structure is expressible solely on the basis of local small scale interactions.

The general characteristics of the large scale structure, as expressed in terms of the small scale orientations of the surface normals, are found to be relatively insensitive to initial conditions applied during simulation. This is consistent with the generally reproducible behavior of global variables such as load, displacement and crack size associated with multiple material specimen or component responses. At the same time, the uniqueness of small scale feature configurations on different material specimen or component fracture surfaces is also evident.

This discussion is organized as follows. First, factors influencing the choice of cellular automata and video imaging as analytical and experimental methods in this investigation are outlined. A description of the experimental arrangement and video imaging are followed by a section on the calibration of the images. A discussion of the cellular automaton formalism is followed by the image processing algorithm which derives the automaton parameters from the

1

experimental images and the calibration database. Discussion of the processed images is followed by the generation of synthetic images and comparison to the processed images.

Approach

The fracture surfaces of metals exhibit diverse features at different scales of observation. Experimental obervations are commonly employed across the full range of scales from the crystal lattice to some portion of the macroscopic component size. The upper limit generally depends on the relative proportion of fracture surface to component size. At crystal lattice scales, fracture is viewed in terms of lattice and grain boundary interactions with irregularities in these structures, e.g. Garrison and Moody [1]. At microstructural scales, fracture is described in terms of transgranular or intergranular paths through a polycrystalline field, e.g. Simmons, Pao and Wei [2] and Harvey, Sudarshan, Louthan and Swanson [3], and brittle cleavage or ductile microvoids, such as discussed by Thompson [4] and Bassim, Klassen, Bayoumi and Wilsdorf [5]. Material damage evolution at or near the the continuum scale, in the form of microvoids and microcracks, as observed by Chermant and Coster [6], Bourcier, Koss, Smelser and Richmond [7] Becker [8] Becker, Smelser, and Richmond [9] and Harvey and Jolles [10] for different stress states and materials, is followed by coalescence at the mezzomechanical scale discussed by Haritos, Hager, Amos, Salkind and Wang [11]. The resulting macroscopic crack growth exhibits the surface features generated by these cumulative effects. Recently, fractal geometry has been examined as a possible method of linking the irregular geometries of fracture across spatial scales by Mandelbrot, Passoja and Paullay [12], Underwood and Banerji [13], Pande, Richards, Louat, Dempsey and Schoeble [14], Pande, Richards and Smith [15] and Dauskardt, Haubensak and Ritchie [16].

The mathematics used to classify and quantify observations at each scale should reflect both the geometric features and analytical forms suggested by the observations. The periodicity and discrete nature of atoms in a body centered cubic, face centered cubic or hexagonal close packed lattice form a concise reference on which to identify and model disturbances associated with substitutions, interstitials, vacancies, dislocations and grain boundaries.

2

Quantum mechanical electron structure calculations are explicitly formulated to reflect these underlying reference structures.

The presence of grain boundaries defines another, somewhat larger scale. Polygons and triangular tesselations, in two dimensions, and polyhedra and tetrahedral tesselations, in three dimensions, are concise topological structures at the grain scale. Micromechanical modeling of trans- and intergranular network models of plastic flow and fracture, which are explicitly linked to these intrinsic geometries, have been examined by Ostoya-Starzewski [17,18].

At continuum scales, associated with statistical averages of the local anisotropy of the lattice and grain scales, continuous and differentiable field models are traditionally employed. These models have evolved around scalar and tensor field descriptions of stress, strain and energy density fields intrinsic to elasticity and phenomonological theories of nonlinear material response. More recently, damage fields have been introduced to include the phenomenological effect of smaller scale features in a continuum formalism (e.g. Kachanov [19]). Computational models, such as finite element, boundary element and finite difference techniques, have developed and incorporated these concepts to facilitate solution of two and three dimensional problems (e.g. Curran, Seaman and Shockey [20] and Nemes [21]). Evolving solutions for nonlinear boundary conditions such as fracture surface generation and contact area size, shape and friction are amenable to formulations at this scale.

Physical measurements of metallic fracture surfaces often suggest the evolution of smaller scale material damage into fracture surface topographies composed of geometric features significantly larger than the continuum scale. The origins of these features lie in the atomic scale lattice inhomogeneities and variations in grain scale sizes and shapes. The material damage evolution is driven by the stress, strain and energy density fields which are sensitive to global load history. Identical locations on two sets of fracture surfaces, generated from two specimens of identical external dimension and subjected to the same load history, are locally unique. Global specimen response, however, is often quite reproducible from specimen to specimen. Therefore, it follows that local differences in material damage evolution may lead to differences on

3

and between fracture surfaces which may not translate into global differences.

The coupling implied by such local and global responses should be evident on the fracture surface at a scale intermediate between the continuum and macroscopic scales. At such an intermediate scale the fracture surface uniqueness should be quantifiable within the context of an appropriate mathematical description. Experimental measurements to support such a description should be of sufficient spatial resolution to delineate local relevant geometric parameters in quantities sufficient to facilitate global comparison in a statistical sense. Such a description should also be able to identify surface equivalence.

The choice of a compact mathematical description to parameterize a three dimensional fracture surface is influenced by the nature of the surface and the information desired from the surface. Exact characterization of each local feature on a surface is one possible objective of parameterization. The identification of dominant types of local features comprising a surface is another. A method of equivalence classification between surfaces is another possible objective. This investigation will focus on the latter two objectives.

As discussed above, the physical nature of the fracture process suggests that the coupling between the local and global repsonses takes place through the local interactions between the material deformation and damage leading to fracture. An appropriate mathematical form to incorporate these effects is a stochastic cellular automaton. Cellular automata, as discussed in detail below, account for local interactions and operate iteratively to generate a global configuration as a set of discrete site values on a mathematical lattice. Such a representation is a compact and efficient method of description and facilitates computational simulations of the fracture surfaces.

The underlying restriction of cellular automata implementation is the need to limit both the size of the parameter set used to describe the lattice sites and the size of the site neighborhood used to account for local interaction. For the purposes of this investigation, the local surface inclination was expressed as a value indicating the nature of orientation, through its local normal, rather

4

than its specific value. Three local surface inclination classes were used: null, principal and diagonal (Figure 1). All were defined (i) with respect to a threshold angle parameter measured from the macroscopic fracture plane (i.e. its elevation) and (ii) the direction of crack growth (i.e. its azimuth).

A null inclination was defined for any local surface orientation for which the angle between the local surface normal and macroscopic surface normal was less than the threshold angle. A principal local surface inclination was defined for orientations exceeding the threshold and being inclined either along or perpendicular to the direction of crack growth. A total of four different local surface inclinations are equivalent and fall under the principal classification by this definition. A diagonal local surface inclination was defined as exceeding the threshold but falling between the principal inclinations. Again, a total of four inclinations are equivalent and classified as diagonal inclinations by this definition.

Given these approaches and definitions, the objective of the this investigation was to examine the global and local relationship between local mezzoscale features of a fracture surface. Video images of the fracture surface were used to set the spatial resolution scale and acquire intensity data from which the surface topography will be assessed. The local surface orientation was characterized from the intensities of the video images by transformation to local surface inclination parameter set at the physical scale corresponding to pixel resolution.

The processed image was used to identify stochastic cellular automata parameters. The use of stochastic cellular automata was motivated by the issues discussed above, i.e. local fracture surface uniqueness and global fracture surface equivalence consistent with global specimen response reproducibility. It also facilitates future modeling and simulation of material damage and fracture surface evolution.
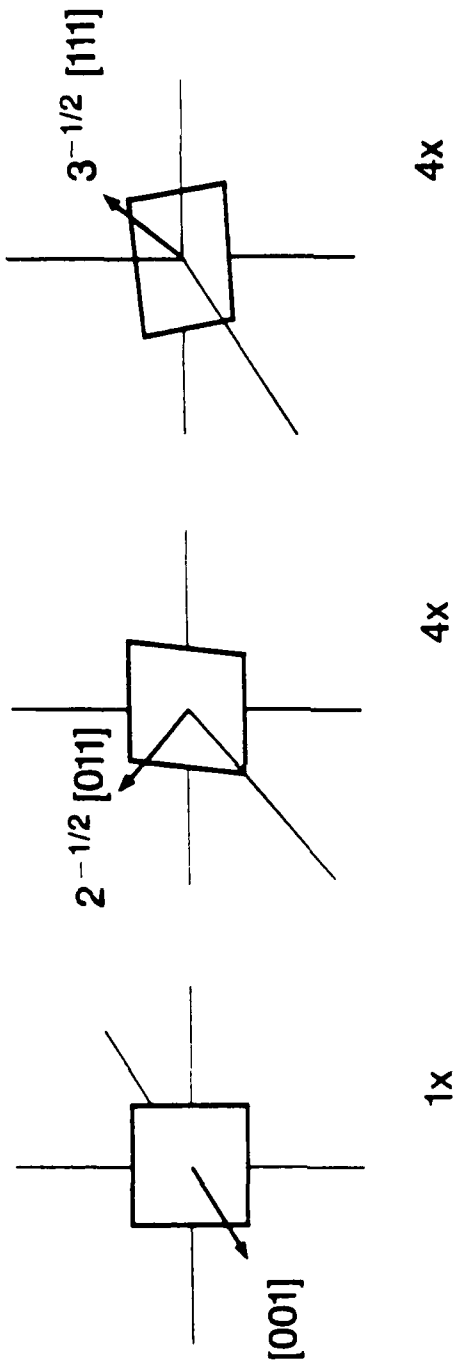
5

Fig. 1 — Definition of null, principal and diagonal facet inclinations

Video imaging configuration

Evolving computational capabilities simultaneously influence theoretical and experimental strategies to support the modeling of physical processes. The use of video imaging for quantitative fractography is an area where the ability to acquire and store visual data in sufficient quantity exists to support the data requirements of computationally intensive modeling paradigms. To address the issues posed at the outset of this investigation, video imaging was used to acquire and store black and white images of an HY-100 compact fracture specimen of standard geometry. The specimen was precracked at room temperature, cooled in liquid nitrogen and rapidly fractured. (It should be noted that a fracture surface generated by any means was amenable to the imaging and subsequent analysis). A 40 by 70 pixel image, covering an 8.41 x 10^{-2} cm^2 area in the center of the fracture surface, was used for this investigation. Each pixel corresponded to approximately 3.04 x 10^{-5} cm^2 of projected area on the fracture surface, or approximately 5.51 x 10^{-3} cm per pixel side.

Each of the 2800 pixel intensities composing the image were stored as 8-bit values providing an intensity range from 0 to 255. These images were processed, in the manner discussed below, to express the local surface topography, on a pixel by pixel basis, in terms of local surface inclination classes. The local surface inclination class, as discussed above, represented null, principal and diagonal inclinations.

The fracture specimen was positioned in line with the optical axis OP of the camera (Figure 2). The plane defined by the fracture surface F, when the fracture surface normal was coincident with the optical axis of the camera, was defined as a fixed reference plane R_F from which specimen rotations were set for the calibration images. The specimen itself could be rotated about either one of two orthogonal axes, i.e. the N-S and the E-W axes. Directions will be specified by angle values for conciseness and common directions, i.e. north (N), south (S), east (E) and west (W), for ease of discussion. The N direction coincided with the direction of crack growth. The N-S axis definition follows immediately. The E and W directions were accordingly transverse to the direction of crack growth and define the E-W axis. Therefore, the axes are
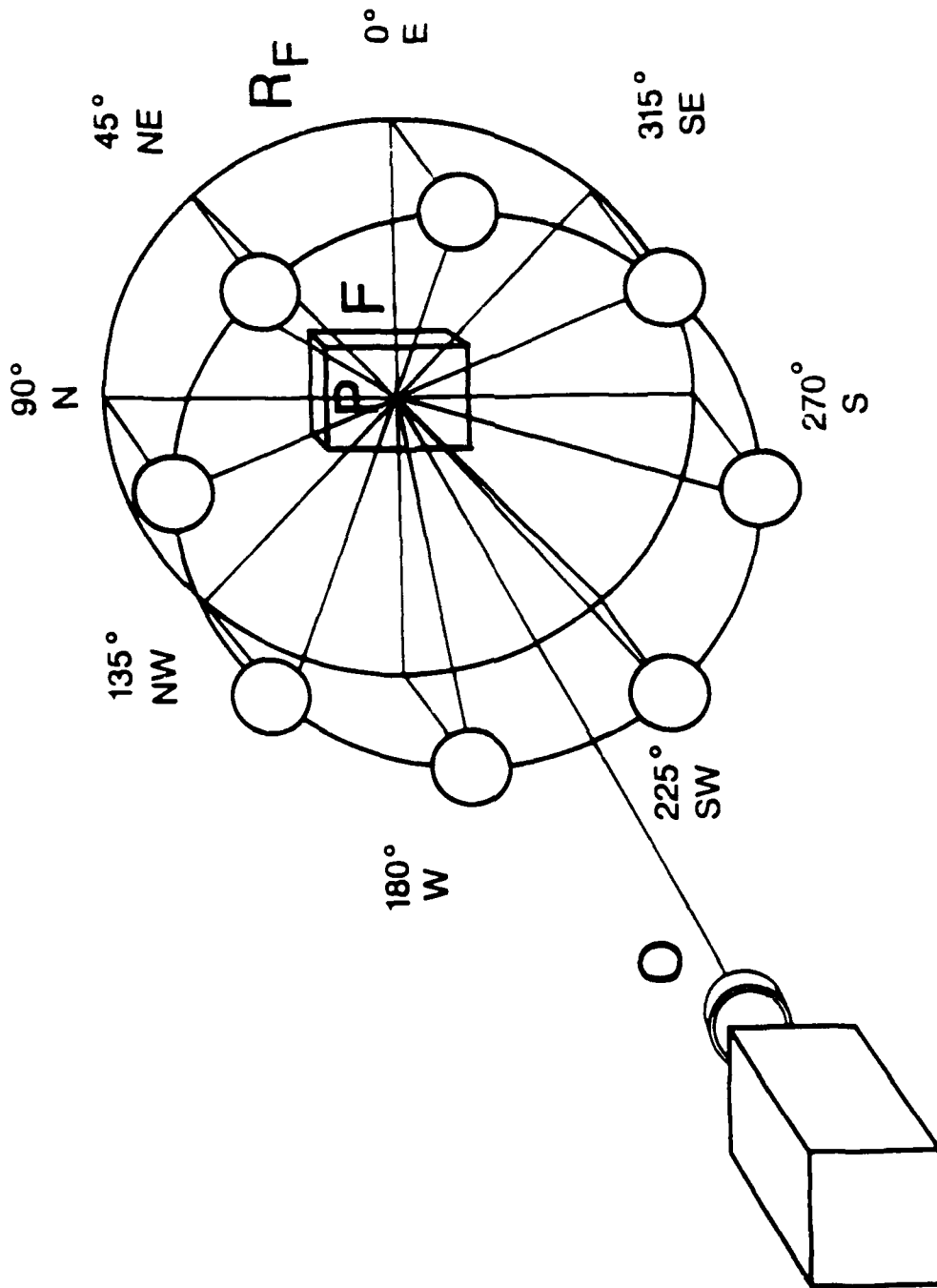
$$\ni = \{ \theta : 0^o , 90^o \} \tag{1}$$

7

Fig 2 -- Schematic diagram of specimen, CCD camera and eight illumination directions φ

o r

$$\Theta = \{ \theta : E\text{-}W , N\text{-}S \} \tag{2}$$

and lie in the reference plane.

Two sets of video images were obtained by a CCD camera. The field of view on the fracture surface is shown in Figure 3. The CCD camera optical axis and fracture surface reference plane normal were parallel. The first set of images, set $C = \{c_{\theta\phi\psi}\}$, were for calibration of grey scale intensities required to obtain local surface orientations. The second set of images, set $Q = \{q_{\phi}\}$, were for processing of pixel intensities into local surface orientations and assignment into local surface inclination classes. The subscript ϕ refers to the illumination source and belongs to the set

$$\Phi = \{ \phi : 0^{o} , 45^{o} , 90^{o} , ... , 225^{o} , 270^{o} , 315^{o} \} \tag{3}$$

o r

$$\Phi = \{ \phi : E , NE , N , ... , SW , W , NW \} \tag{4}$$

The subscript ψ refers to the calibration orientation and belongs to the set

$$\Psi = \{ \psi : -45.00^{o} , -33.75^{o} , -22.50^{o} , ... , 22.50^{o} , 33 75^{o} , 45.00^{o} \}$$

$$\tag{5}$$

Illumination of the fracture surface for the calibration and processing images was provided by one of eight different light sources in the illumination set $L = \{l_{\phi}\}$. The selection of the particular light source was consistent with the requirements of the calibration and processing procedures described in detail below. The light sources were mounted in a coplanar, evenly spaced circular pattern (Figure 2). The positions of the light sources in the light source plane R_L coincided with the E, NE, N, NW, W, SW, S, and SE directions define similarly to those on the fracture surface reference plane R_F. The normal to the light
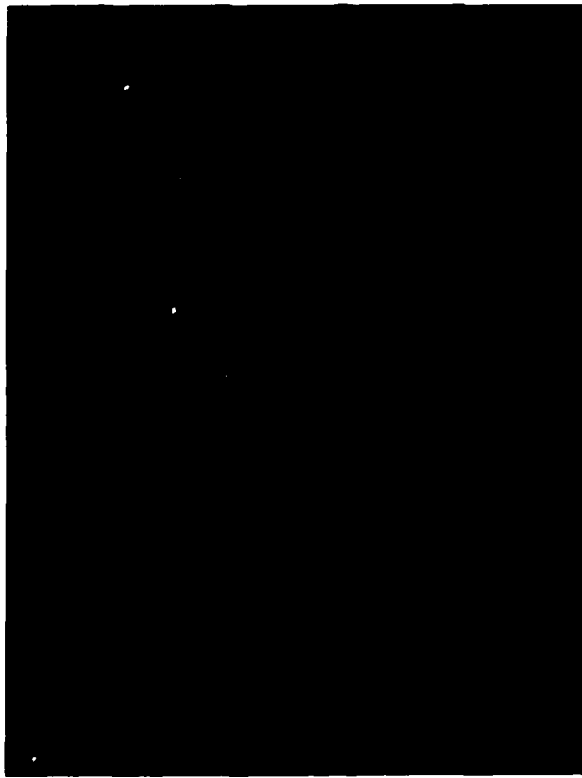
Fig 3   Video image of fracture surface   Crack growth direction is from bottom,
toward top of image

source plane was positioned to lie on the optical axis O of the camera. The light source plane was placed at a distance away from the fracture surface plane so that each source was positioned at an elevation of 45° with reference to the point defined by the optical axis O and the fracture surface reference plane R_F. Illumination azimuth was therefore controlled by source selection while the elevation was fixed.

Each pixel of a fracture surface image, i.e. $c_i{}^t{}_{,\theta\phi\psi}$ or $q_i{}^t{}_{,\theta}$, was the image of a small, local section of the fracture surface. The i and t variables denote the local directions parallel and perpendicular to the crack front. These coincide with the N-S and E-W axes, respectively. The calibration pixel intensities were influenced by specimen rotation ψ (Figure 4) around the θ axes and illumination source ϕ. Preliminary studies of the fracture surface demonstrated its local pixel scale and global image scale diffusivity toward incident light. This was used for calibration and processing in such a manner that no assumptions on the specific character of the diffusivity were required. Surfaces of a more specular nature, while not studied in this investigation, could also be amenable to study in their natural state or by appropriate deposition of a thin diffusive coating which would not alter the surface at the scales of interest defined by pixel resolution.

Calibration Procedure

Calibration of the fracture surface, through the image set C, was required to establish reference intensities with which to compare the intensity of images for processing on a pixel by pixel basis. A number of different approaches have been used to address the characterization of surface geometry from two-dimensional images of reflected surface intensity, as discussed in the collection of approaches to this class of problem edited by Horn and Brooks [22]. In many applications, such as terrain mapping and image recognition, only a single image or a pair of stereo images are available. The object being viewed is generally not under the control of the observer. The approach in this investigation drew on some of the concepts employed in the study of these problems while taking advantage of the ability to acquire images of the fracture surface in different orientations. Fracture surface orientation was
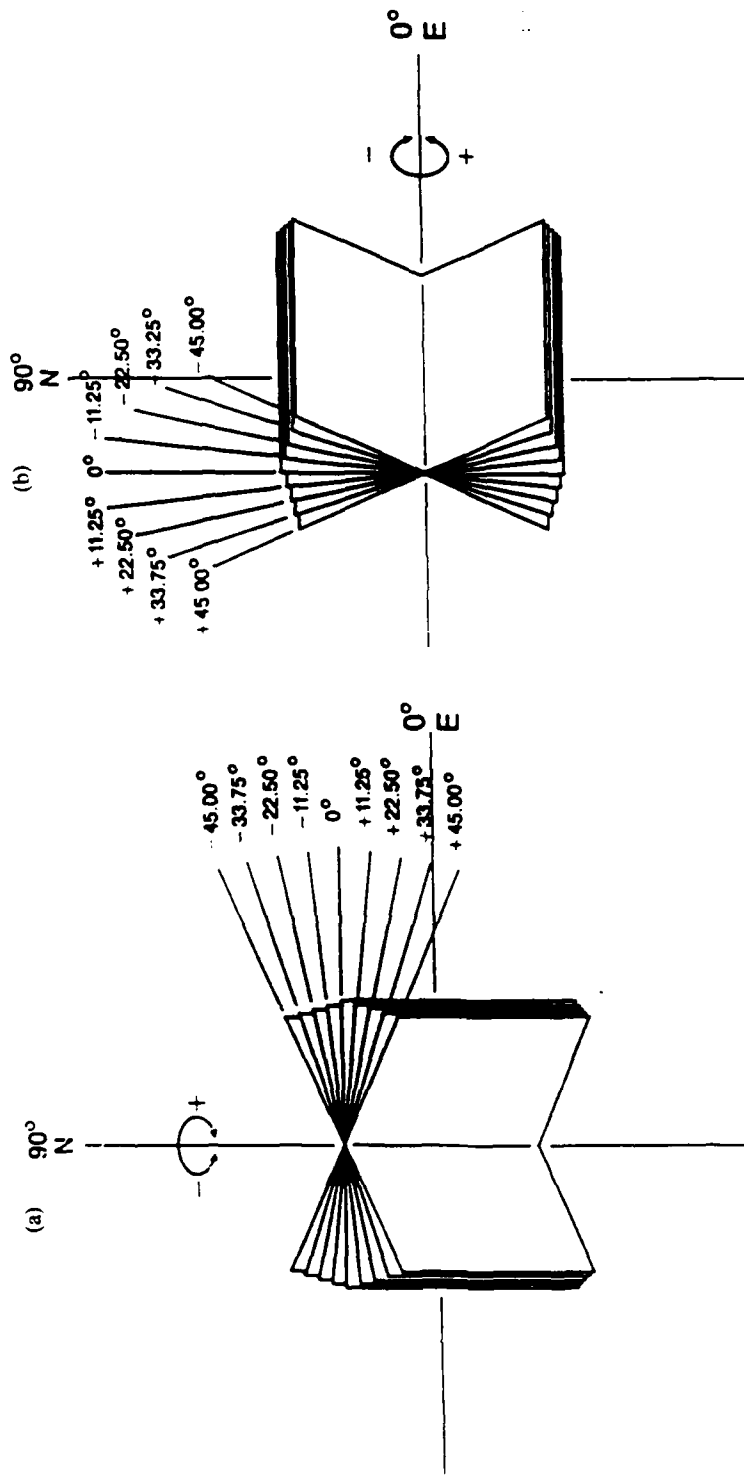
11

Fig. 4 — Schematic diagram of specimen rotations Ψ, used for calibration, around specimen rotation axis θ (a) vertical and (b) horizontal

12

varied by rotation of the specimen with respect to the N-S axis and by rotation with respect to the E-W axis. Different conceptual approaches to the calibration problem are reviewed along with the actual approach implemented in this investigation.

In principle, a local fracture surface calibration would compare pixel intensities against reference values associated with the pixel itself. These could be constructed for each pixel by illuminating the fracture surface from different directions while maintaining a constant distance and orientation from light source to surface to ensure constant incident intensity. An intensity calibration over both illumination azimuth and elevation would be obtained for each pixel. This requires the camera and fracture specimen to move as a system if the light sources are fixed, or the light sources to move if the camera and fracture surface system are fixed, in order to maintain correspondence between each pixel and an associated local region of the fracture surface through multiple image acquisitions. Practical difficulties were associated with being able to move either the video camera and fracture specimen as a unit or being able to move the light sources. Although this approach was not used in this investigation, a system to do this is currently under development.

An alternative to the pixel intensity calibration procedure would be to achieve a global surface intensity calibration. Local intensities would be compared against a reference values reflecting an average intensity incorporating the contributions of the entire region under consideration. Conceptually, such a calibration could be obtained by moving the camera to a sufficiently large distance away from the specimen such that the region of interest on the fracture surface would be imaged in only one pixel. The illumination source could again be positioned relative to the specimen and camera to cover the required range of azimuth and elevation. The difficulty of moving the camera to a sufficiently far distance and imaging the fracture surface region of interest on a single pixel are obvious.

A practical solution to the calibration problem was implemented by acquiring images with the specimen at various rotations about each rotation axes. In his manner both the camera and the light sources were stationary. Processing of

13

pixel intensity values $c_i{}^t{}_{,\theta\phi\psi}$ was performed for each pixel in each image. Each image was defocused by replacing the center pixel value of all three pixel by three pixel subimages by the average of the nine pixel values. This is, essentially, a low pass spatial filter. Thus, an essentially uniform intensity distribution over the fracture surface region of interest was achieved. This process was analogous to the far field calibration described above. Direct global averaging of the pixels to a value $c_{\theta\phi\psi}$ were found to approximate the successive local averaging procedure. On this basis, direct global averaging was adopted for purposes of surface calibration.

Calibration images were obtained for specimen rotations about the E-W and N-S axes. For each of the eight illumination directions ϕ and two specimen rotation axes θ, nine specimen orientations ψ ranging from -45° to $+45^\circ$ in 11.25° increments were illuminated and stored for a total of 144 calibration images. The projected area of the fracture surface region of interest varied since the specimen was positioned in front of the fixed camera. The image processing region was modified for each image to contain only the region of interest on the fracture surface.

The calibration curves obtained from this global averaging procedure are shown in Figure 5. The curves are plotted for a constant illumination direction, with respect to the fracture surface plane and direction of crack growth, from measurements taken at the different fracture surface orientations about the vertical and horizontal axes. Linear interpolation is used to link together the nine specimen rotation values for each illumination direction.

The anticipated monotonic decline of the illumination intensity $c_{\theta\phi\psi}$ is apparent as the fracture surface normal vector is rotated away from light source direction. An example is the E illumination calibration curve for the the specimen rotation about the vertical N-S axis. Essentially constant illumination intensity is apparent for light source directions and specimen rotation axes defining a plane perpendicular to the plane defined by the specimen normal vectors as the plane is rotated. The N illumination calibration curve for the vertical specimen rotation axis is an example. The *intermediate illumination directions, such as NE*, exhibit an attenuated

14
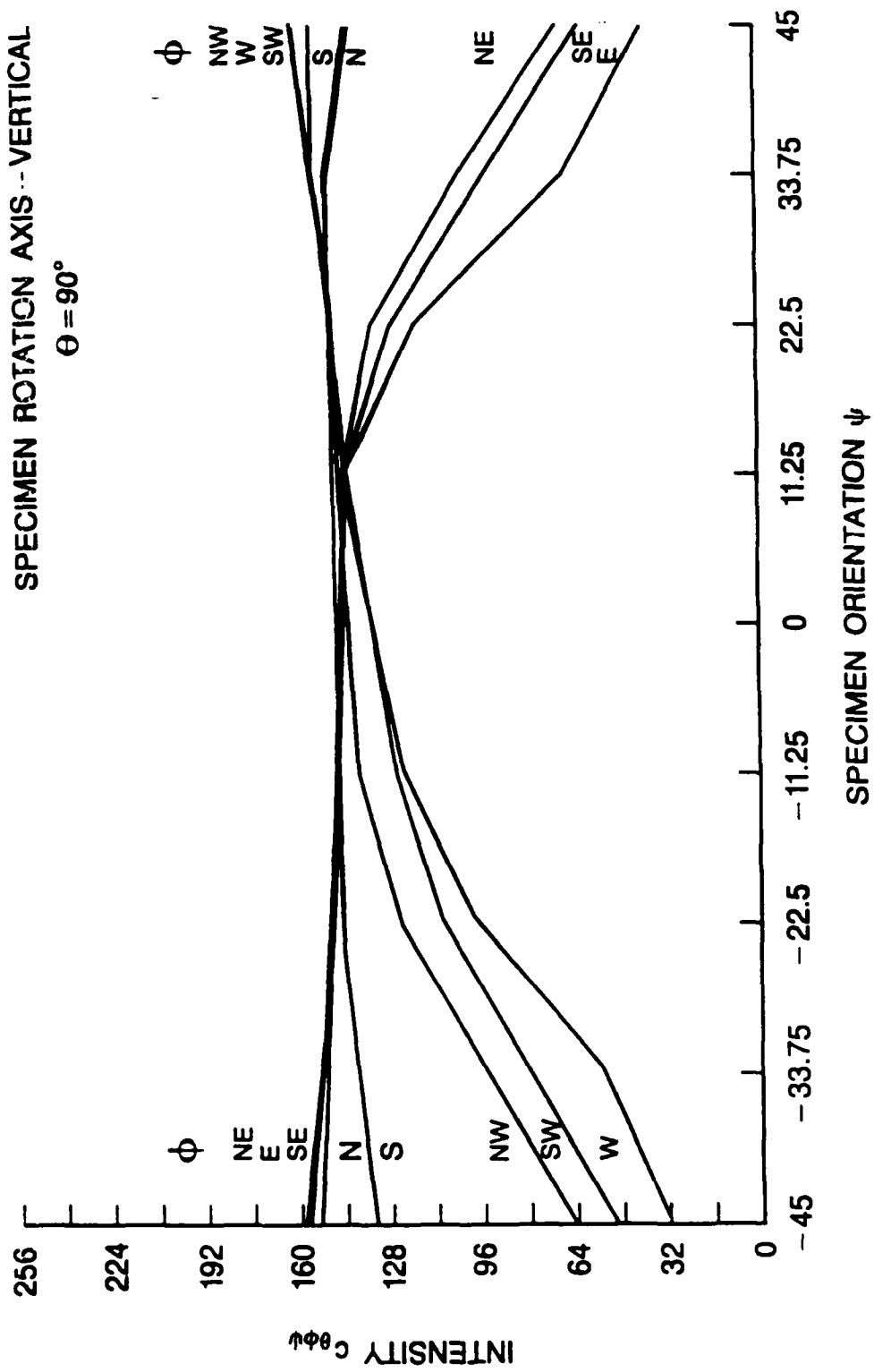
Fig. 5 — Intensity versus specimen orientation calibration curves for eight light sources. Specimen rotation about (a) vertical axis.

(a)
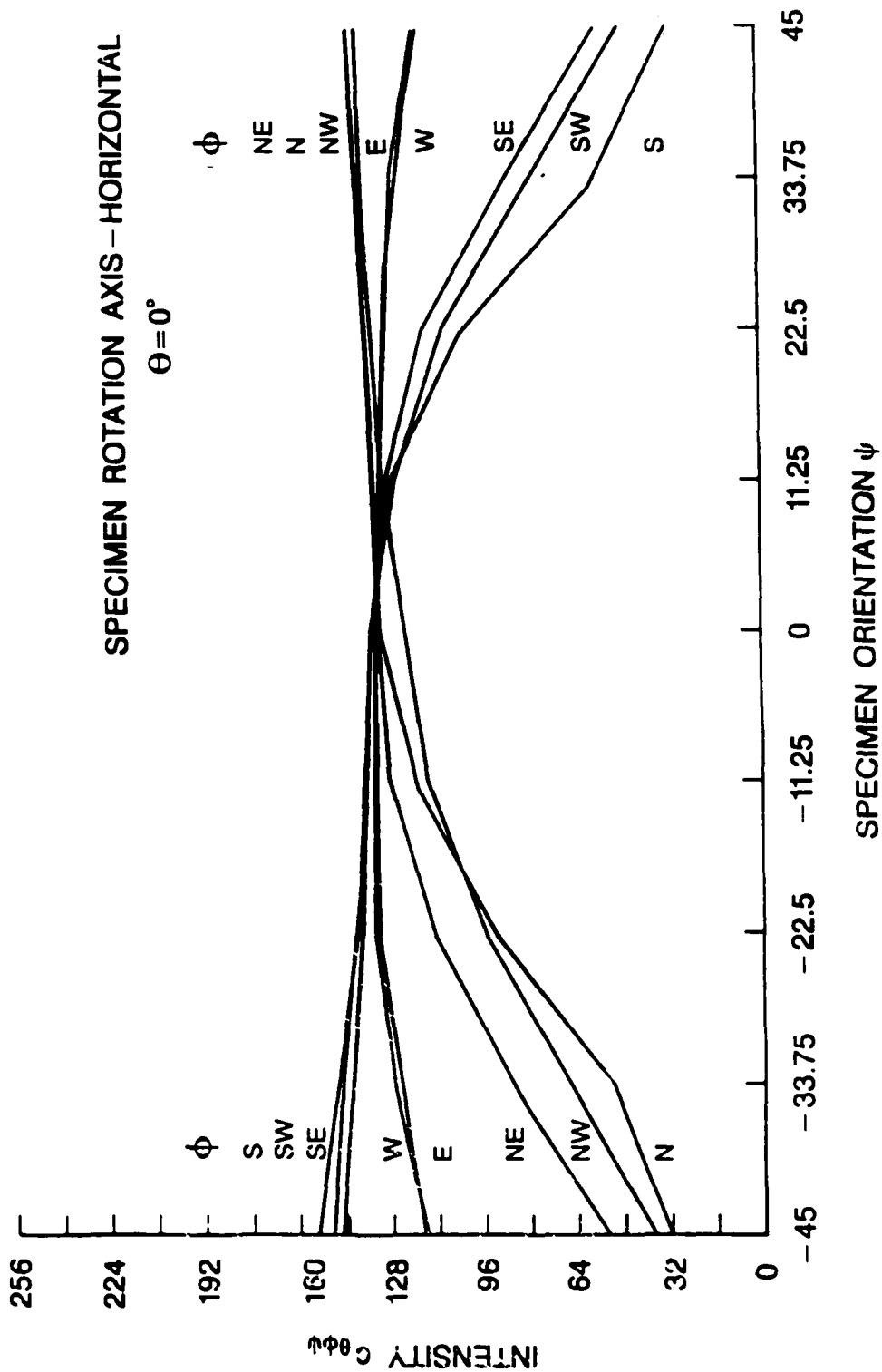
Fig. 5 — (Continued) Intensity versus specimen orientation calibration curves for eight light sources. Specimen rotation about (b) horizontal axis.

(b)

16

monotonic decline as the fracture surface is rotated away from the light source direction. Symmetry and antisymmetry of magnitude and slope is clearly produced between appropriate pairs of calibration curves as expected for the proper combinations of specimen rotation axis and illumination direction.

Cellular automata theory

Cellular automata were discussed by von Neumann [23,24] in order to study the complexity and means by which objects, assembled from simple components, could self-replicate within a large system. The discrete nature of cellular automata in both space and time provides a large number of identical sites in space whose time evolution is governed by identical local neighborhoods of adjacent sites. These sites are usually arranged in a periodic lattice. Simple rules govern the synchronous evolution of each possible neighborhood at the current time to a new site value at the next value of time. The value of each site on the resulting lattice in space and time is drawn from a finite set of site values. The outcome for each possible neighborhood configuration may be unique, in the case of deterministic cellular automata, or drawn from all possible values in a nonuniform manner, as in the case of stochastic cellular automata. Large scale digital computation and computer graphics has made the study of large, synchronous systems more accessible, facilitating interest in modeling paradigms such as cellular automata. A brief review of cellular automata follows in order to introduce stochastic cellular automata for this investigation.

Deterministic cellular automata (e.g. Wolfram [25]) and stochastic cellular automata (e.g. Grinstein, Jayaprakash and Y. He [26] , Kinzel [27], Kaneko and Akutsu [28]) may be formulated on lattices whose site values form a finite set. Define $x_i{}^t$ to be the site value at position i and time t. The site values are defined by the set X of k integers as

$$X = \{ x : 0, 1, \ldots, k\text{-}1 \} \qquad (6)$$

so that

17

$$x_i^t \in X \qquad\qquad\qquad (7)$$

Site values at time t+1 are governed by an automaton rule which maps the preceding neighborhood configuration at time t into the new site value at time t+1 (For a spatial radius r equal to one, the neighborhood is shown in Figure 6). The "radius" of the spatial neighborhood is defined as r.

In the deterministic case

$$x_i^{t+1} = F[\ x_{i-r}^t\ ,\ x_{i-r+1}^t\ ,....,\ x_i^t\ ,....,\ x_{i+r-1}^t\ ,x_{i+r}^t\ ] \qquad (8)$$

o r

$$x_i^{t+1} = F[\ y_i^t\ ] \qquad\qquad\qquad (9)$$

where y_i^t is the neighborhood configuration number, i.e.

$$y_i^t = \sum_{j=0}^{2r} k^{2r-j}\ x_{i-r+j}^t \qquad\qquad (10)$$

A total of 2r+1 sites compose each site neighborhood at time t. The configuration of the x_i^t neighborhood governs x_i^{t+1} through the application of the rule F. The value of y_i^t is contained in a set Y defined by the size k of the set X and the neighborhood radius r, i.e.

$$Y = \{\ y : 0\ ,\ 1\ ,\ ....,\ k^{2r+1}\ \} \qquad\qquad (11)$$

so that

$$y_i^t \in Y \qquad\qquad\qquad (12)$$

The neighborhood configuration number is a useful representation when implementing the cellular automaton rule in tabular form. The table required for a deterministic cellular automaton would be a list k^{2r+1} elements long, i.e.
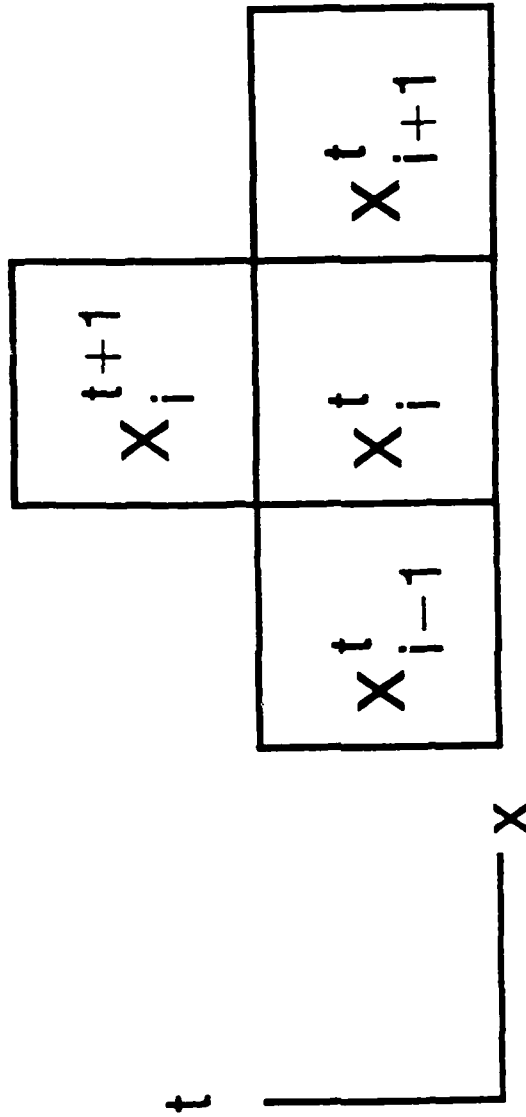
18

Fig. 6 — Cellular automation neighborhood for neighborhood r = 1 and times t and t + 1

one outcome for each element y of neighborhood configuration set Y. Tabular implementation is also computationally efficient and admits all possible rules.

The exponential growth of neighborhood configurations with neighborhood radius generally constrains the size of the set X for statistical and computational reasons. The coarseness of the set X and the neighborhood configuration size are offset by the large number of rule iterations which govern the lattice site values. A site value depends on the site values contained in a space-time cone which converges on the site value through increasing time. Simultaneously, a site value affects any site in a space-time cone which expands through increasing times.

In the case of stochastic cellular automata, the site value set X and finite spatial neighborhood are identical to those defined for deterministic cellular automata. The configuration y_i^t formed by the x_i^t neighborhood, however, is associated with a set of probabilities $p_{y,x}$ governing the generation of the site value x_i^{t+1}. The value of x_i^{t+1} generated from the neighborhood configuration will not be unique, which differs from deterministic cellular automata. The stochastic cellular automata rule P is

$$x_i^{t+1} = P[\ x_{i-r}^t,\ x_{i-r+1}^t,....,\ x_i^t,....,\ x_{i+r-1}^t,x_{i+r}^t\ ;$$
$$p_{y,0},\ p_{y,1},\ \cdots,\ p_{y,k-2},\ p_{y,k-1}\ ] \qquad (13)$$

o r

$$x_i^{t+1} = F[\ y_i^t\ ;\ p_{y,x}] \qquad (14)$$

The probabilities for each neighborhood y must satisfy the requirement that

$$p_{y,0} + p_{y,1} + ...+ p_{y,k-2} + p_{y,k-1} = 1. \qquad (15)$$

The table required for a stochastic cellular automaton would be an array of k^{2r+1} rows and k columns, representing the probability of each possible outcome for each neighborhood configuration in set Y.

Stochastic cellular automata for fracture surface image processing

The fracture surface is physically generated in a sequential manner as the crack propagates. The propagation direction defines a direction of increasing time and a complimentary direction of constant spatial position. The two dimensional spatial domain in the video images may, therefore, also be interpreted as the time evolution of an essentially one-dimensional linear portion of the crack front as it propagated into the solid and generated the crack surface. Lines of constant time may be considered parallel to the crack front, while lines of constant position would be orthogonal to the lines of constant time. For the video images in this investigation, constant time is in the horizontal direction, time is increasing in the upward direction and constant position is in the vertical direction.

Within the context of the stochastic cellular automata formalism described above, the specific form used for the fracture surface analysis is defined. The local surface inclination class value at a site on the surface will be the site value x_i^t. The inclination values are defined by the set X of three integers

$$X = \{ x : 0, 1, 2 \} \tag{16}$$

where 0 is null, 1 principal and 2 diagonal local inclinations.

A finite spatial neighborhood of radius of $r=1$ was selected to investigate the transition of local inclination class x_i^t to x_i^{t+1}. Therefore, the neighborhood configuration number, according to Equation 10,

$$y_i^t = 2^2 x_{i-1}^t + 2^1 x_i^t + 2^0 x_{i+1}^t \tag{17}$$

A total of three sites compose each site neighborhood at time t. From Equation (11) a total of 27 neighborhood configurations are possible. The set of probabilities $p_{y,x}$ governing the transition of site x_i^t to x_i^{t+1} will be examined using the video images and the form of the stochastic rule P, which is now

$$x_i^{t+1} = P[\, x_{i-1}^t, x_i^t, x_{i+1}^t ; p_{y,0}, p_{y,1}, p_{y,2} \,] \tag{18}$$

21

o r

$$x_i^{t+1} = P[\ y_i^t\ ;\ p_{y,0}\ ,\ p_{y,1}\ \cdot\ p_{y,2}\ ]\qquad\qquad (19)$$

The probabilities for each neighborhood y satisfy the requirement that

$$p_{y,0} + p_{y,1} + p_{y,2} = 1.\qquad\qquad (20)$$

As discussed above, the definition of three inclination values does not uniquely specify the fracture surface topography. Rather, it defines and distinguishes between the classes of inclinations on the surface. It should be noted that if construction of the actual surface topography was desired, this could be accomplished by other methods.

Image processing algorithm

The set Q of eight images was obtained for processing with respect to the set C of calibration curves. Each of the eight images were obtained using a different light source from the set L. The fracture surface plane F was normal to the optical axis O for all eight fracture surface images. Reduction of the eight images to the processed image of the surface was based on a three step procedure to identify the local surface inclination class at each pixel from the null, principal and diagonal inclinations defined previously (Figure 7).

The first step of the procedure used the calibration curves to transform the pixel intensities q_i^t from values ranging from 0 to 255 to a value of 0 or 1 with respect to a threshold inclination angle ψ_{th} selected by the user. A set of threshold angles was chosen to uniformly span a range from zero to null saturation. For this investigation, the range was from 0° to 20° at 4° increments. The threshold inclination has an associated threshold intensity associated with each calibration curve (Figure 8). As discussed above, six calibration curves for each of the two specimen rotation axes exhibited sensitivity to specimen rotation. These twelve curves were paired with the appropriate fracture surface image according to illumination direction.
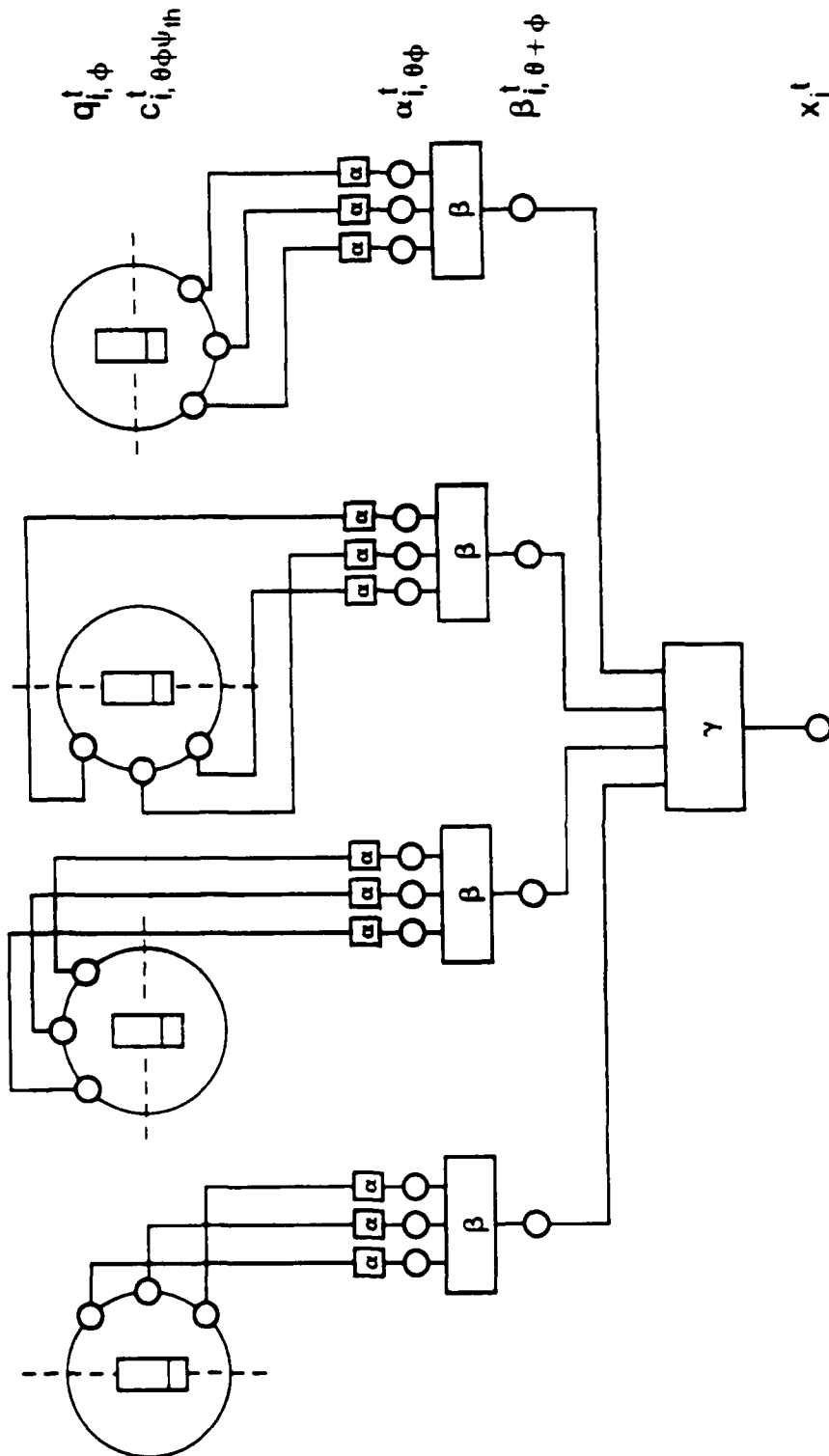
22

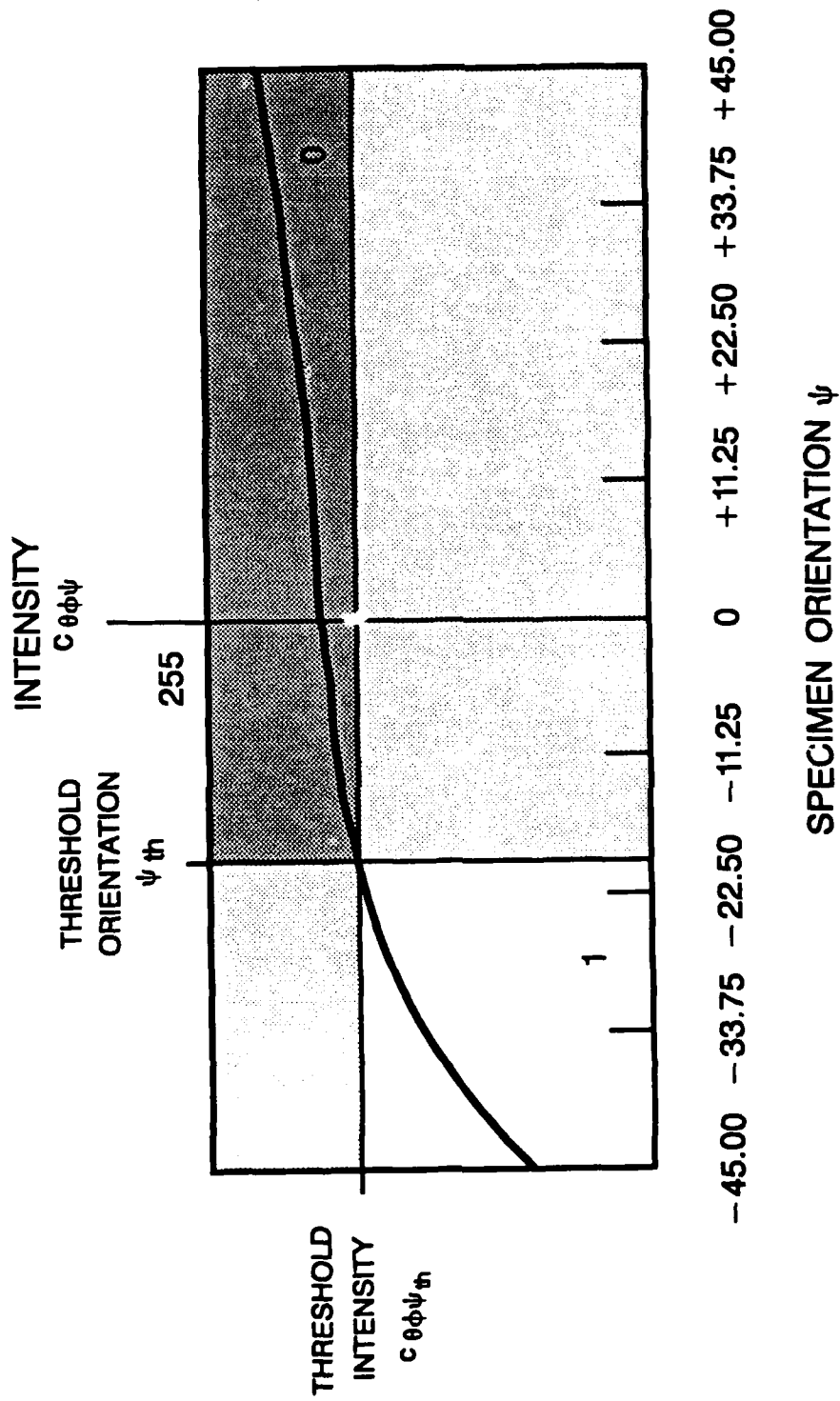Fig 7   Schematic of pixel intensity to local surface inclination transformation

Fig. 8 — Schematic of illumination and orientation threshold values applied to mapping of nonlinear intensity versus specimen orientation data to binary value

Higher pixel intensity indicated an orientation toward the illumination source. The shape of the calibration curve was sufficiently nonlinear to identify orientation away from the illumination source which exceeded the threshold inclination. Decreasing sensitivity of the calibration curve, corresponding to increased inclination in the direction of illumination, did not support discrimination between inclination smaller than the threshold inclination and inclination greater than the threshold in the direction of the illumination.

The intensity of each pixel in each of the eight images was compared with its associated calibration curve intensity, consistent with its sensitivity to inclination away from the illumination source, i.e.

$$\alpha_{i}^{t},_{\theta\phi} = \alpha \left[q_{i}^{t},_{\phi} \cdot c_{i}^{t},_{\theta\phi}\psi_{th} \right] \tag{20}$$

$$\theta = 0^{\circ}, 90^{\circ} \tag{21}$$

$$\phi = \theta - 45^{\circ}, \theta, \theta + 45^{\circ},$$
$$(\theta + 180^{\circ}) - 45^{\circ}, (\theta + 180^{\circ}), (\theta + 180^{\circ}) + 45^{\circ} \tag{22}$$

If the pixel intensity was greater than the threshold intensity, the pixel was given a transformed intensity value of 0. If the pixel intensity was less than the threshold intensity, a transformed value of 1 was assigned. A value of 0 indicated no apparent inclination of the pixel field with respect to the threshold. A value of 1 indicated significant inclination with respect to the threshold value. Through this process, each portion of the region of interest on the fracture surface associated with a pixel was characterized by twelve binary values grouped into four three-bit words.

The second step in the image processing sequence examined the $\alpha_{i}^{t},_{\theta\phi}$ binary values to assess whether these attributes are consistent with the four possible principal inclinations. These binary values were considered in sets of three adjacent $\alpha_{i}^{t},_{\theta\phi}$ values, as summarized in Figure 9, for each principal direction which would be considered. A concensus for a candidate principal direction was defined according to a majority rule. Each of the four three-bit binary
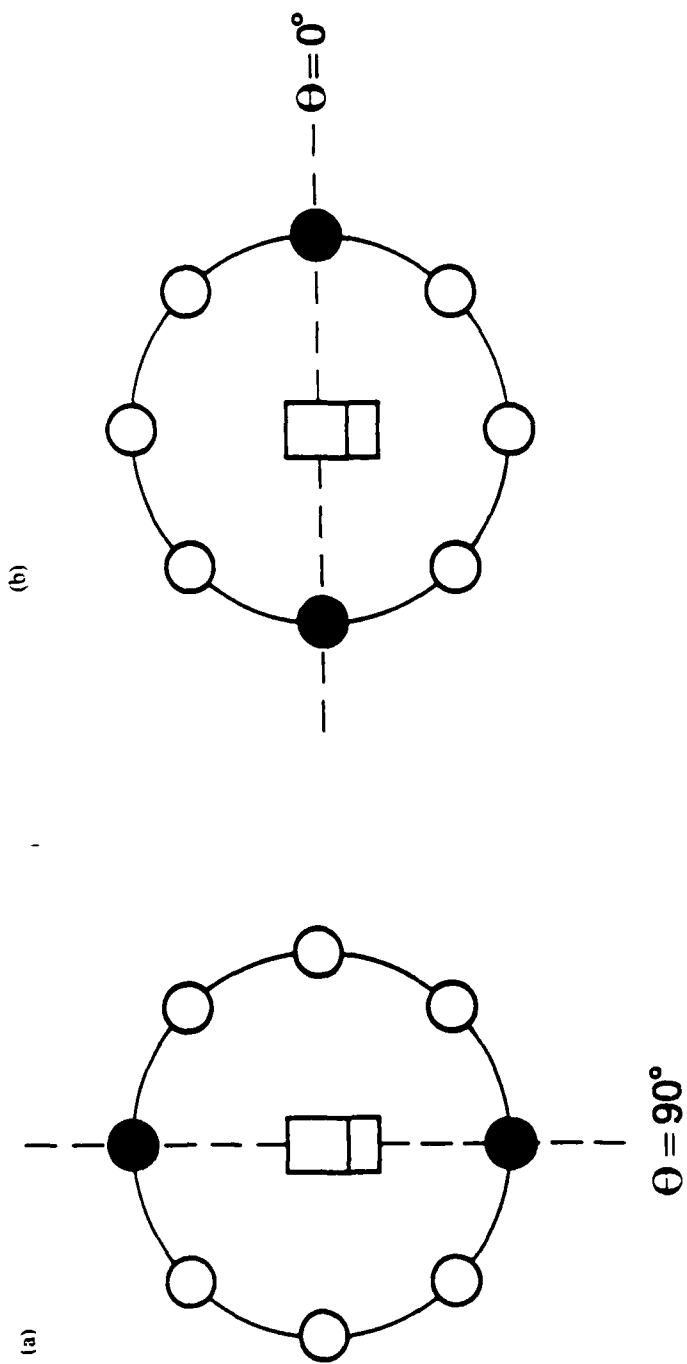
Fig. 9 — Schematic of inclination binary value transformation to candidate principal inclinations. Two sets of three illumination directions about (a) vertical and (b) horizontal.

words were transformed to a single four-bit binary value in this manner (Table 1), i.e.

$$\beta_i{}^t_{,\theta+\phi} = \beta\left[\alpha_i{}^t_{,\theta\ \phi-45^o} , \alpha_i{}^t_{,\theta\ \phi} , \alpha_i{}^t_{,\theta\ \phi+45^o} \right] \tag{23}$$

$$\theta = 0^o , 90^o \tag{24}$$

$$\phi = \theta , \theta+180^o \tag{25}$$

Each binary value was associated with one of the four possible principal directions.

The third image processing step examined the symmetries of the four possible principal inclinations in order to arrive at consistent representations of the null, principal and diagonal inclination classes from these values. The assignment of an inclination class to each pixel was based on the rotational asymmetry of the $\beta_i{}^t_{,\theta+\phi}$ indicators (Figure 10), i.e.

$$x_i{}^t = \gamma\left[b_i{}^t_{,0^o} , b_i{}^t_{,90^o} , b_i{}^t_{,180^o} , b_i{}^t_{,270^o} \right] \tag{26}$$

Four null values suggest a null inclination class. One prinipal value and three null values suggests a principal inclination class. Two principal values and two null values suggest a diagonal inclination class if asymmetrically distributed. Two principal values, if symmetrically distributed, offer no concensus and therefore suggest a null inclination. Three out of four or four out of four principal inclination values are inconsistent with a well defined principal inclination and are taken to be null inclination. In this way, the four-bit binary word argument is transformed to a 1-bit ternary word indicating inclination class (Table 2).

Discussion of Processed Images

For purposes of presentation, the null, principal and diagonal inclination values were represented by red, green and blue colors, respectively. Six

27

$\alpha_i^t{}_{,\theta\phi}$	$\beta_i^t{}_{,\theta+\phi}$
000	0
001	0
010	0
011	1
100	0
101	1
110	1
111	1

Table 1 — Transformation of 3-bit binary inclination words to 1-bit binary candidate principal inclination value by majority rule

28
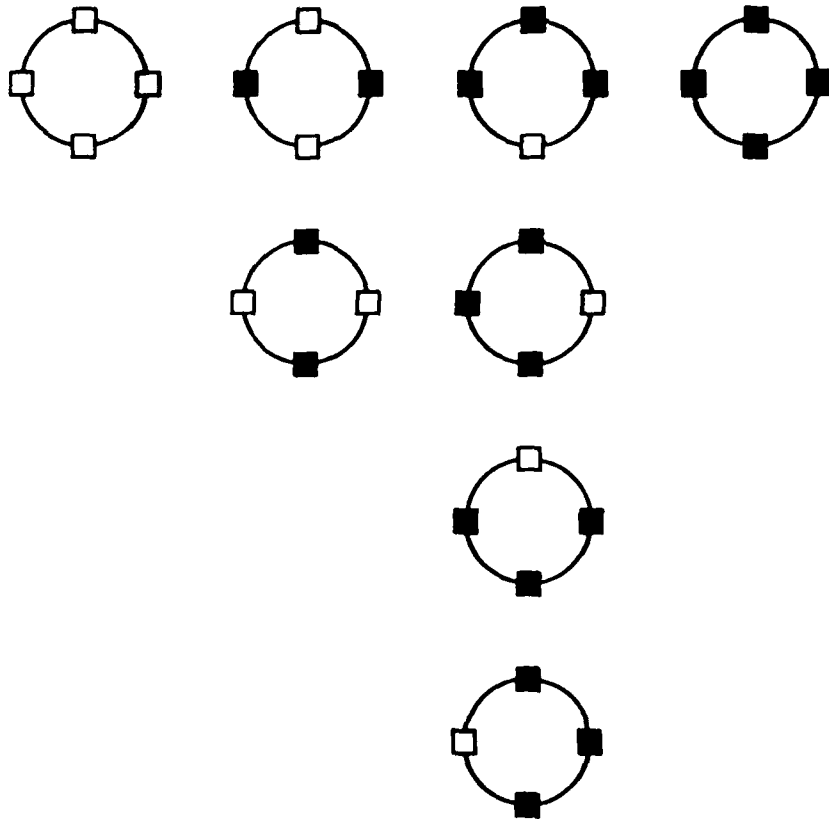
$$x_i{}^t = 0 \quad \text{(NULL)}$$

(a)

Fig. 10 — Transformation of candidate principal inclinations to (a) null inclinations

29
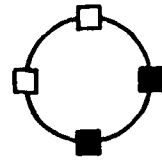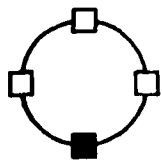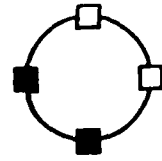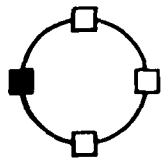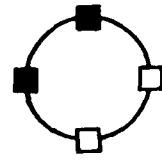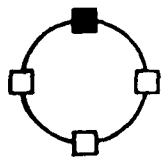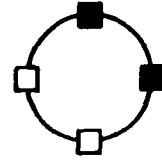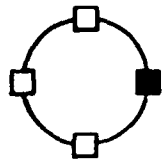
$x_i^t = 1$ (PRINCIPAL) $x_i^t = 2$ (DIAGONAL)

(b)   (c)

Fig. 10 — (Continued) Transformation of candidate principal inclinations to (b) principal and (c) diagonal inclinations

30

$\beta_{i,\theta+\phi}^t$	x_i^t
0000	0
0001	1
0010	1
0011	2
0100	1
0101	0
0110	2
0111	0
1000	1
1001	2
1010	0
1011	0
1100	2
1101	0
1110	0
1111	0

Table 2 — Transformation of 4-bit binary candidate principal inclination word to 1-bit ternary inclination value from symmetry considerations

processed images were generated for threshold angles ψ_{th} values from 0° to 20° at 4° increments. The processed images are displayed in the bottom row of Figure 11.

Threshold angles near 0° presented an ambiguous state to the algorithm. The threshold decision in the image processing algorithm would theoretically be based on identical or nearly identical intensity values for each pixel since at 0° threshold all such images are, in principle, degenerate. Noise in the calibration curves dominated the threshold decision at small threshold angles.

As the threshold angle increased, geometric structure emerged on the processed images. The processed images demonstrated a complex geometric grouping of local inclination classes on the fracture surface. As the threshold inclination angle was increased, the processed image tended to a uniform null inclination. The image becomes increasingly saturated by the red color assigned to pixels of null inclination. This was consistent with the classification of each pixel site as a null inclination with respect to the reference plane R. The null inclination, therefore, functions as a reference and background upon which principal and diagonal inclinations are superimposed.

The dominant trend at the intermediate values of threshold inclination angle (over the range considered) is for principal inclinations , indicated by green, to be grouped together as "islands" on the null inclination "sea" of red. The blue diagonal inclination class never appears as isolated structures on the null background. All blue features exist as aggregate forms on the green principal inclination structures in the processed image. In fact, relatively few instances of blue-red boundaries exist. This implies that the diagonal inclinations are coupled to the principal inclinations in a secondary role for this particular fracture surface.

Whether the diagonal inclinations are a cause, an effect or a combined influence on the formation of the fracture surface cannot be inferred from the basis of this data. The relative proportion and relationship of diagonal inclination areas to principal inclination areas suggest that the diagonal inclination sites are dominated by smaller scale features which disrupt, in

32

RANDOM FIELD (p_0, p_1, p_2)

STOCHASTIC RULE

RANDOM SEED (p_0, p_1, p_2)

STOCHASTIC RULE

PROCESSED PHYSICAL SEED

PROCESSED PHYSICAL IMAGE

0°   4°   8°   12°   16°   20°   24°   28°
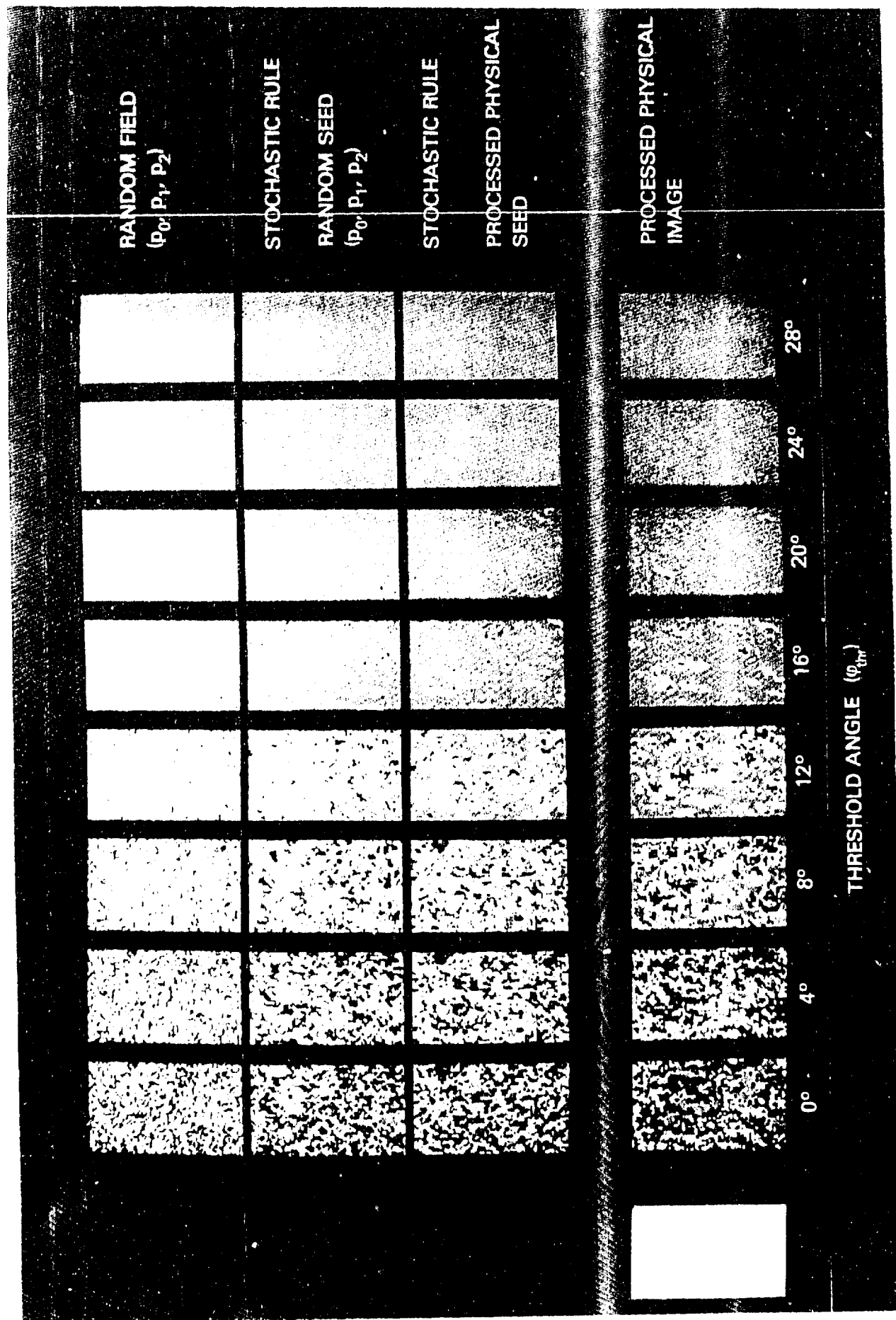
THRESHOLD ANGLE (φ_{thr})

Fig. 11 — The processed fracture surface image, a processed seed synthetic processed image, a random seed synthetic processed image and a random image for threshold angles of tan 0°, 4°, 4° (a) 8°, (b) 12°, (c) 16°, (d) 20°.

33

some manner, the principal inclination features on the fracture surface run parallel to the direction of crack growth. The diagonal inclination sites would appear to be spatially infrequent but capable of strong local action. Closer examination of these sites by higher resolution fractographic methods could provide additional insight into the relationship between microstructural and mezzostructural features.

The stochastic cellular automaton rule for each value of the threshold angle was constructed by tabulating the x_i^{t+1} as outputs for each y_i^t neighborhood configuration as input. The three tabulated outputs for each neighborhood configuration were normalized. Therefore, the probabilities in each row summed to unity, according to Equation (15). Only two of the probabilities in each row were independent. Each resulting rule table featured 27 rows, one for each possible input configuration, and 3 columns, one for each possible output. Each value in the table was the probability that the input configuration of the row would produce the output configuration of the column. Each table contained 54 independent parameters.

Of the 27 neighborhood configurations, nine are symmetric under spatial reflection. The remaining eighteen can be divided into nine pairs of asymmetric configurations which map into one another under spatial reflection. The physical nature of the fracture surface, as captured by the stochastic cellular automaton, was examined by performing a two factor analysis of variance on the three output occurrences associated with each asymmetric neighborhood configurations pair. A two row by three column table was created for each of the nine neighborhood configuration pairs. The rows corresponded to the input configurations and the columns to the output site values. Symmetry conditions suggest that the output probabilities associated with 001 and 100 input configurations, for example, should be equal. F factors for the row variance to random variance ratio, obtained for each neighborhood pair at each value of the threshold angle, were in 42 of 45 cases insufficient to reject a null hypothesis of symmetric behavior at a 0.05 significance level (Table 3). In one case, at high threshold angle, the tabulated data would not support an analysis of variance. obtained from the processed images These results suggest that the aggregate local physical symmetry of the

34

Spatial Neighborhood Pairs	Threshold Angle				
	0°	4°	8°	12°	16°
100 001	1.210	0.945	0.070	0.336	0.010
200 002	0.810	0.703	1.324	4.000	0.429
110 011	0.379	0.203	0.886	0.031	0.000
210 012	0.000	2.526	2.685	3.692	0.308
120 021	1.414	1.923	0.324	0.671	4.000
220 022	0.039	0.631	0.111	0.164	--
201 102	0.045	0.540	1.000	2.077	1.000
211 112	0.338	16.000	6.950	0.027	0.000
221 122	1.316	10.246	25.000	0.387	0.000

Table 3 — Two factor analysis of variance F values for row variance to random variance ratio. Significance level of 0.05, indicating departure from translational symmetry with respect to neighborhood configuration, corresponds to F value of 18.5.

surface is supported by the data from the processed images and the stochastic cellular automata formalism.

Generation of synthetic images

If the stochastic cellular automata formalism successfully captures the small scale interactions and large scale structure of the fracture surface, iterative application of the automaton should be able to generate synthetic processed images. Different initial conditions, in terms of site values at zero time and random number sequences implementing the rule probabilities, were considered in order to examine the robustness of the stochastic cellular automata. Essential features of the processed image, such as the relative proportions of null, principal and diagonal inclination classes, the self organization between inclination classes and the connectivity between inclination class regions all indicate the ability of the stochastic cellular automata formalism to efficiently and compactly capture the essence of the surface topology.

Two types of synthetic processed images were generated. In the first type of synthetic processed image, the zero time row of the processed physical image was used to seed the zero time row of the synthetic image. Random number sequences were used to support the rule table probability decisions required by the automaton. For the second type of processed image, the zero time row of the synthetic image was seeded by random initial values in the same proportions exhibited by the processed image. Random number sequences were again used to support the required rule probability decisions. The synthetic processed images are shown in the second and third rows of Figure 11. The self organization and similarity of the aggregate structures in the processed and synthetic images are apparent. (One synthetic image is shown for each case in Figure 11. Five images for each case, further illustrating the similarity of image structures, are shown in the Appendix.)

A set of red, green and blue random images is also shown in the top row of Figure 11 for reference and comparison. The random images color proportions were selected to be equal to the color proportions of the respective processed

image. The departure of the processed and synthetic processed images from randomness is evident.

Concluding remarks

Experimental measurement of local fracture surface inclination were obtained from a set of video images for intensity versus orientation calibration and a set of video images for processing. The images for processing were mapped to a set of inclination classes consistent with null, principal and diagonal inclinations defined with respect to the macroscopic surface normal and crack growth direction.

The global character of the surface, in terms of local interactions between null, principal and diagonal inclination classes, was examined through identification of stochastic cellular automaton parameters from the processed image of local inclination classes. The automaton output probabilities corresponding to input neighborhood configurations equivalent under spatial reflection were found to be similar. Physical consistency of the parameters with respect to symmetry under spatial reflection was therefore demonstrated.

Synthetic processed images were generated using two different types of initial conditions. The first set of synthetic processed images, referred to as processed seed synthetic processed images, were generated from the processed local inclination values at the zero time sites. The image boundary corresponded to the direction in which crack propagation generated the surface in the image field. The stochastic cellular automaton probabilities were invoked with a random number sequence to arrive at the output decision for each input local neighborhood configuration. A total of five different processed seed synthetic images were generated.

The second set of synthetic processed images, referred to as random seed synthetic processed images, were generated from zero time sites using random seeding in proportion to the processed image local inclination class probabilities. Output decisions for these synthetic images were also obtained using random number sequences. Five random seed synthetic images were

generated from five different sets of initial conditions and five different random number sequences.

The processed and synthetic processed images exhibited features similar to those of the processed image obtained from experimental data. All three types of images show considerable self organization of the local inclination classes when compared to random images.

The processed and synthetic processed images demonstrate the size and shape of local inclination class aggregation on the fracture surface. The fracture surface is a manifestation of the underlying antecedant damage processes at a smaller scale in the material. The information transport in the stochastic cellular automaton reflects a balance between the strength of the small scale local interactions, defined by the input neighborhood, and the persistence of large scale damage structures which have evolved from these interactions

Metallic fracture surfaces are complex geometric structures. The spatial scales defining material damage and fracture are evolving scales. Both are simultaneously united at the instant of surface generation. The material damage evolution is frozen by the very fracture event which it precipitates while the fracture surface is defined by the aggregate state of the damage at fracture. The ability to identify the dominant local interaction scale and the global scale of self-organization from experiment should complement analytical modeling of the fracture process. This method of analysis serves to identify extraordinary features on an already complex background for additional scrutiny by higher resolution experimental methods.

References

[1] Garrison, W. M. Jr., and Moody, N. R., The Influence of Inclusion Spacing and Microstructure on the Fracture Toughness of the Secondary Hardening Steel AF1410. Met. Trans. A 18, 1257-1263 (1987).

[2] Simmons, G. W., Pao, P. S. and Wei, R. P., Fracture Mechanics and Surface Chemistry of Subcritical Crack Growth in AISI 4340 Steel. Met. Trans. A 9, 1147-1158, (1978).

[3] Harvey, D. P. II, Sudarshan, T. S., Louthan, M. R. and Swanson, R. E., Corrosion Fatigue Behavior of 90/10 Copper-Nickel Cladding for Marine Structures. J. Mat. Energy Sys. 7, 269-275 (1985).

[4] Thompson, A. W., The Relation Between Changes in Ductility and in Ductile Fracture Topography: Control by Microvoid Nucleation. Acta Metall 31, 1517-1523 (1983).

[5] Bassim, M. N., Klassen, R. J,. Bayoumi, M. R. and Wilsdorf, H. G. F., Fracture Topography of HSLA Steels. Mat. Sci. Engng. 92, 107-111 (1987).

[6] Chermant, J. L. and Coster, M., Quantitative Fractography. J. Mat. Sci. 14, 509-534 (1979).

[7] Bourcier, R. J., Koss, D. A., Smelser, R. E. and Richmond, O., The Influence of Porosity on the Deformation and Fracture of Alloys. Acta. Metall. 34, 2443-2453 (1986).

[8] Becker, R., The Effect of Porosity Distribution on Ductile Fracture. J. Mech. Phys. Solids 35, 577-599 (1987).

[9] Becker, R., Smelser, R. E. and Richmond, O., The Effect of Void Shape on the Development of Damage and Fracture in Plane-Strain Tension. J. Mech. Phys. Solids 37, 111-129 (1989).

[10]   Harvey, D. P. II and Jolles, M. I., Correlations between Micromechanical Features and Material Toughness in HY-100 Steel. J. Mat. Sci. Engng. 10, 262-272, (1988).

[11]   Haritos, G. K., Hager, J. W., Amos, A. K., Salkind M. J. and Wang, A. S. D., Mezzomechanics: The Microstructure-Mechanics Connection. Int. J. Solids and Struct. 24, 1081-1096 (1988).

[12]   Mandelbrot, B. B., Passoja, D. E. and Paullay, A. L., Fractal Character of Fracture Surface of Metals. Nature 308, 721-722 (1984).

[13]   Underwood, E. E. and Banerji, K., Fractals in Fractography. Mat. Sci. and Engng 80, 1-14 (1986).

[14]   Pande, C. S., Richards, L. E., Louat, N., Dempsey, B. D. and Schoeble, A. J., Fracture Characterization of Fracture Surfaces. Acta Metall. 35, 1633-1637 (1987).

[15]   Pande, C. S., Richards, L. R. and Smith, S., Fractal Characteristics of Fractured Surfaces. J. Mat. Sci. Lett. 6, 295-297 (1987).

[16]   Dauskardt, R. H., Haubensak, F. and Ritchie, R. O., On the Interpretation of the Fractal Character of Fracture Surfaces. Acta Metall. Mater.38, 143-159 (1990).

[17]   Ostoya-Starzewski, M., Damage in Random Microstructure: Size Effects, Fractals and Entropy Maximization. Appl. Mech. Rev. 42, No. 11, Part2 (1989).

[18]   Ostoya-Starzewski, M., Mechanics of Damage in a Random Granular Microstructure: Percolation of Inelastic Phases. Int. J. Engng. Sci. 27, 315-326 (1989).

[19]   Kachganov, L. M., Introduction to Continuum Damage Mechanics. Martinus Nijhoff, The Netherlands (1986).

[20] Curran, D. R., Seaman, L. and Shockey, D. A., Dynamic Failure in Solids. Physics Today, 46-55 (1977).

[21] Nemes, J. A. and Eftis, J., Rate Dependent Modelling of Multidimensional Impact and Post-Spall Behavior, Proc. Int. Conf. Shock-Wave and and High-Strain-Rate Phenomena in Materials, San Diego, 1990.

[22] Horn, B. K. P. and Brooks, M. J. (eds.), Shape from Shading. MIT Press, Cambridge (1989).

[23] von Neumann, J., The General and Logical Theory of Automata. in Collected Works, J. von Neumann, A. H. Taub, ed., (1963).

[24] von Neumann, J., Theory of Self-Replicating Automata, A. W. Burks, ed. University of Illinois, Urbana (1966)

[25] Wolfram, S., Universality and Complexity in Cellular Automata, Physica 10D, 1-35 (1984).

[26] Grinstein, G., Jayaprakash, C. and He, Y., Statistical Mechanics of Probabilistic Cellular Automata. Phys. Rev. Lett. 55, 2527-2530 (1985).

[27] Kinzel, W., Phase Transitions in Cellular Automata. Z. Phys. B 58, 229-244 (1985).

[28] Kaneko, K. and Akutsu, Y., Phase Transitions in Two-Dimensional Stochastic Cellular Automata. J. Phys. A 19, L69-L75 (1986).

Appendix

Tabulated data from each processed image, for each threshold angle value considered, is provided in Table A1. These tables were used to determine the parameters for the stochastic cellular automata. The stochastic cellular automata rules was constructed by normalizing the x_i^{t+1} as outputs with respect to the y_i^t neighborhood configuration as input.

As discussed in the main text, two types of synthetic processed images were generated. In the first type of synthetic processed image, the zero time row of the processed physical image was used to seed the zero time row of the synthetic image. For the second type of processed image, the zero time row of the synthetic image was seeded by random initial values in the same proportions exhibited by the processed image. Random number sequences were used to support the rule table probability decisions in both cases. Five synthetic images of each type, based on the stochastic rule parameters derived from the processed images for each value of the threshold angle, are shown in Figure A1. The self organization and similarity of the aggregate structures in the processed and synthetic images were found to be relatively insensitive to the random number seed or to the initial conditions used.

y	n_0	n_1	n_2	$\sum_i n_i$
0	208	51	34	293
1	90	32	17	139
2	73	19	19	111
3	18	25	9	52
4	34	55	18	107
5	24	32	19	75
6	11	4	14	29
7	13	21	28	62
8	28	16	58	102
9	75	36	12	123
10	33	21	5	59
11	26	6	7	39
12	31	55	25	111
13	22	121	37	180
14	20	61	33	114
15	13	9	25	47
16	9	14	21	44
17	23	48	70	141
18	73	17	37	127
19	10	6	10	26
20	24	5	19	48
21	15	30	18	63
22	21	62	35	118
23	12	17	14	43
24	22	18	88	128
25	15	35	66	116
26	25	50	158	233
	968	866	896	2730

Table A1 — Tabulated output site values with respect to input neighborhood configurations for threshold angles of (i) 0°

y	n_0	n_1	n_2	$\sum_i n_i$
0	394	35	57	486
1	30	17	9	56
2	120	14	47	181
3	14	13	7	34
4	8	17	20	45
5	17	17	16	50
6	33	14	31	78
7	12	15	32	59
8	39	32	95	166
9	37	14	16	67
10	16	9	5	30
11	23	8	8	39
12	18	20	15	53
13	16	30	25	71
14	16	33	21	70
15	13	12	18	43
16	7	9	19	35
17	21	19	74	114
18	113	10	50	173
19	13	9	14	36
20	38	11	33	82
21	15	17	18	50
22	9	36	38	83
23	17	29	24	70
24	43	18	110	171
25	13	21	70	104
26	53	49	182	284
	1148	528	1054	2730

Table A1 — (Continued) Tabulated output site values with respect to input neighborhood configurations for threshold angles (ii) 4°

y	n_0	n_1	n_2	$\sum_i n_i$
0	395	58	12	465
1	135	49	9	193
2	45	9	11	65
3	28	43	8	79
4	62	114	21	197
5	15	21	8	44
6	4	5	6	15
7	12	15	15	42
8	16	23	23	62
9	116	60	10	186
10	45	33	10	88
11	18	7	4	29
12	40	101	30	171
13	51	185	41	277
14	18	56	26	100
15	11	13	24	48
16	11	17	16	44
17	8	28	44	80
18	44	11	17	72
19	17	9	6	32
20	14	7	6	27
21	14	28	16	58
22	12	39	20	71
23	5	15	8	28
24	12	19	37	68
25	6	27	42	75
26	7	35	72	114
	1161	1027	542	2730

Table A1 — (Continued) Tabulated output site values with respect to input neighborhood configurations for threshold angles of (iii) 8°

46

y	n_0	n_1	n_2	$\sum_i n_i$
0	975	83	7	1065
1	197	48	7	252
2	20	5	3	28
3	35	47	4	86
4	60	112	11	183
5	19	14	6	39
6	1	4	1	6
7	6	9	4	19
8	2	10	3	15
9	174	56	6	236
10	26	12	3	41
11	1	4	1	6
12	46	110	23	179
13	48	177	10	235
14	6	31	9	46
15	6	8	12	26
16	5	12	9	26
17	1	14	23	38
18	20	6	4	30
19	8	4	3	15
20	5	0	2	7
21	12	14	1	27
22	9	27	9	45
23	1	3	0	4
24	5	3	13	21
25	4	13	15	32
26	2	6	15	23
	1694	832	204	2730

Table A1 — (Continued) Tabulated output site values with respect to input neighborhood configurations for threshold angles of (iv) 12°

47

y	n_0	n_1	n_2	$\sum_i n_i$
0	2037	57	3	2097
1	127	14	0	141
2	7	0	0	7
3	36	35	0	71
4	34	38	1	73
5	3	4	0	7
6	1	0	0	1
7	2	3	2	7
8	0	0	0	0
9	111	33	0	144
10	6	2	0	8
11	0	0	0	0
12	25	44	4	73
13	5	49	3	57
14	0	7	0	7
15	1	3	1	5
16	0	2	6	8
17	0	0	1	1
18	3	1	0	4
19	1	0	0	1
20	0	0	1	1
21	2	7	0	9
22	4	2	1	7
23	0	0	0	0
24	0	0	0	0
25	0	1	0	1
26	0	0	0	0
	2405	302	23	2730

Table A1 — (Continued) Tabulated output site values with respect to input neighborhood configurations for threshold angles of (v) 16°
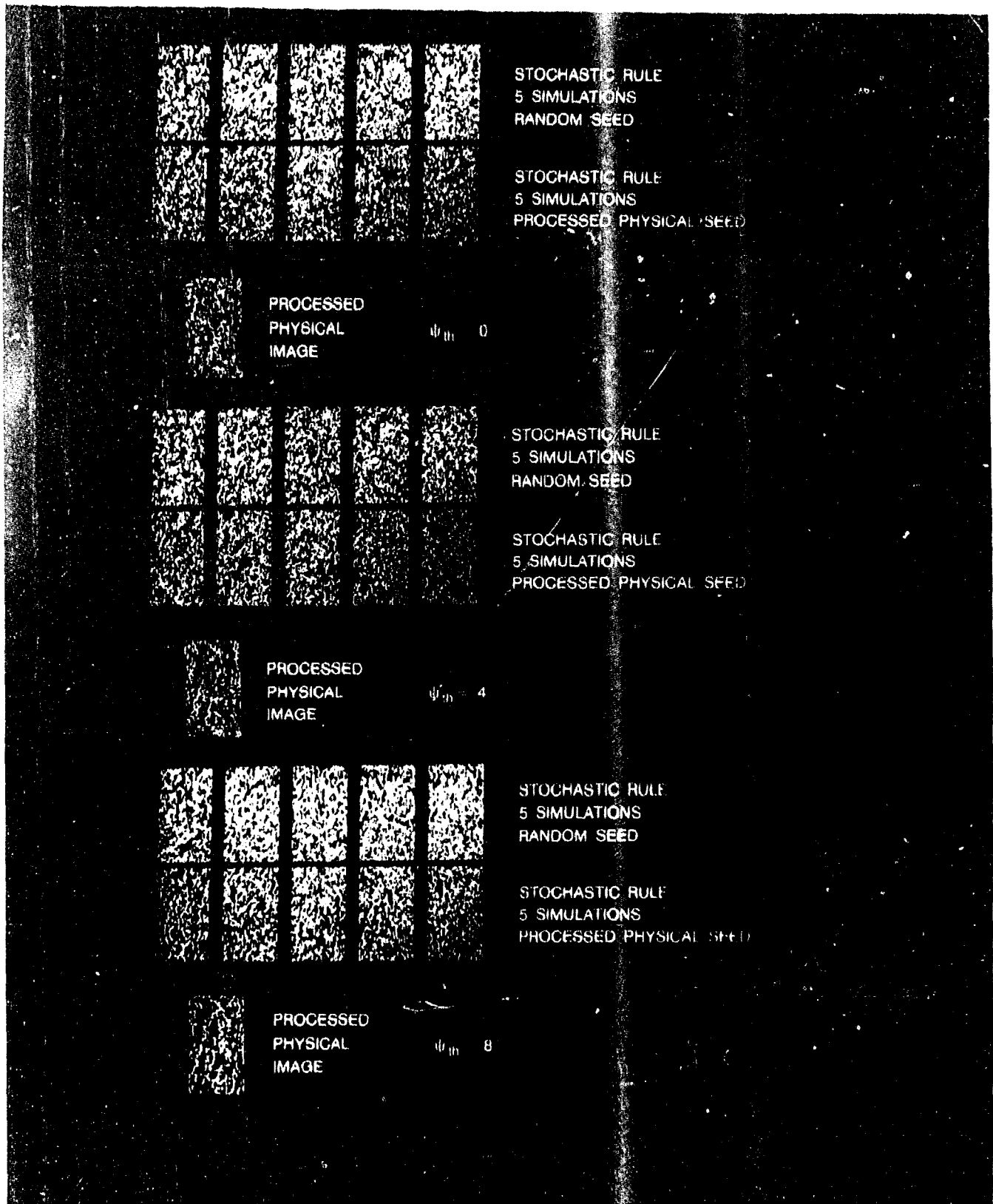
Fig. A1   The processed fracture surface image, five processed seed synthetic processed images and five random seed synthetic processed images are shown for threshold angles of (a) 0°, (b) 4°, (c) 8°
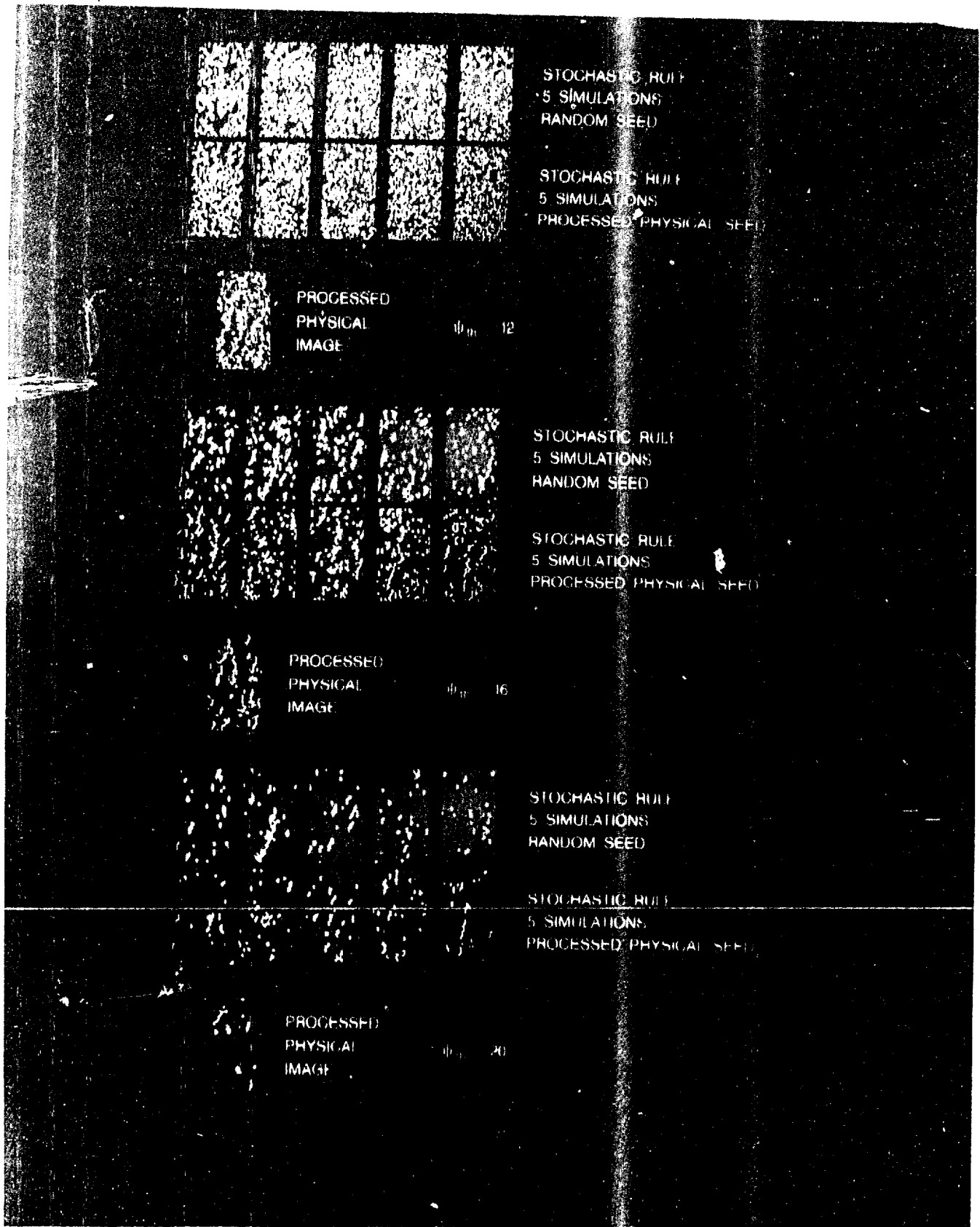
Fig. A1 (Continued) The processed fracture surface image, five processed seed synthetic processed images and five random seed synthetic processed images are shown for threshold angles of (d) 12°, (e) 16°, (f) 20°